RESEARCH ARTICLE



Check for updates

Constrained flash sintering of gadolinium-doped ceria thin layers

Luca Balice¹ Apurv Dash^{1,2} | Christian Melcher³ Doris Sebold¹ | Robert Mücke¹ | Alexander Opitz³ | Martin Bram^{1,4} | Olivier Guillon^{1,5} |

Correspondence

Luca Balice, Forschungszentrum Jülich GmbH - Institute of Energy Materials and Devices - IMD-2, 52428 Jülich, Germany. Email: l.balice@fz-juelich.de

Funding information

Deutsche Forschungsgemeinschaft, Grant/Award Numbers: GU 933/9-2. BR3418/1-2; Austrian Science Fund, Grant/Award Number: 10.55776/I5478

Abstract

Flash sintering is a novel technology, which enables densification of ceramics in seconds to minutes at moderate furnace temperatures. To date, it has mostly been demonstrated on samples with simple geometries like dog bones, bars, or cylinders, which are quite far from real applications. In the present work, we extend flash sintering to gadolinium-doped ceria (GDC) thin ceramic layers $(\sim15\times8\times0.008~\text{mm}^3)$ screen printed onto rigid alumina substrates. Building on our previous work with GDC dog bones, we selected the same material due to its relevance for solid oxide cell applications. All experiments were performed isothermally under voltage-to-current control mode. Flash sintering was triggered under relatively high electric fields (> 500 V cm⁻¹), current densities (> 600 mA mm⁻²), and furnace temperatures (> 1100°C), as indicated by the characteristic abrupt increase in the specimen's conductivity and bright light emission. However, significant effects of the electric current were observed at a furnace temperature of 1200°C, with current densities above 800 mA mm⁻², and a dwell time of 180 min, leading to relative densities above 90%, compared to only 75% for conventional sintering under the same temperature and time. The harsher conditions needed to flash sinter these specimens are explained by the very high aspect ratio (surface area-to-volume) compared to other usual geometries in flash sintering experiments. In addition, the heat dissipation in the special experimental setup plays an important role in terms of energy balance.

KEYWORDS

constrained sintering, flash sintering, gadolinium-doped ceria, solid oxide cells, thin films

INTRODUCTION 1

Solid oxide cells (SOCs) are electrochemical devices and are among the multiple green solutions to address the growing global energy demand. Their fundamental structure consists of two porous electrodes separated by a dense electrolyte layer. The electrochemical reactions take place in the electrodes at the triple phase boundaries, where the respective reaction gases, ionic conducting, and electronic conducting phases are in contact. On the other hand, the

This is an open access article under the terms of the Creative Commons Attribution License, which permits use, distribution and reproduction in any medium, provided the original work is properly cited.

© 2025 The Author(s). Journal of the American Ceramic Society published by Wiley Periodicals LLC on behalf of American Ceramic Society.

J Am Ceram Soc. 2025;108:e70033.

¹Forschungszentrum Jülich GmbH -Institute of Energy Materials and Devices - IMD-2, Jülich, Germany

²Department of Energy Conversion and Storage, Denmark Technical University, Lyngby, Denmark

³Department of Chemistry, Technical University Vienna, Vienna, Austria

⁴Institut für Werkstoffe Lehrstuhl Werkstofftechnik Ruhr Universität Bochum Universitätsstraße 150, Bochum, Germany

⁵JARA-Energy Jülich Aachen Research Alliance, Jülich, Germany

<u> Journal</u>

electrolyte conducts only O²⁻ ions and must prevent the direct mixing of the reaction gases.¹ If the cell is operated as a solid oxide fuel cell, the chemical energy of the fuel gas, typically hydrogen or hydrocarbons, is converted into electrical energy.² In reverse operation, the same cells are able to efficiently produce hydrogen or other fuel gases as energy carriers by means of electrolysis and are, therefore, referred to as solid oxide electrolysis cells.³

The production of planar SOCs can involve different processes such as tape casting, screen-printing, thermal spraying, and thin-film methods, such as dip or spin coating, physical vapor deposition, pulsed laser deposition, and others.^{4,5} In addition to the complex processes, a primary challenge derives from the sintering of multilayered ceramics. For SOCs sintering, the following challenges must be addressed:

- 1. Different materials in contact can generate stresses during heating/cooling stages, due to a mismatch of the coefficient of thermal expansion or due to a differential shrinkage rate during sintering.⁶
- 2. High sintering temperatures are often incompatible with supporting structures (e.g., metal substrates) and increase the risk of decomposition and evaporation of volatile elements, like Mn, especially in the case of long dwell times.
- 3. High sintering temperatures can trigger undesired reactions, such as the formation of an electrically insulating SrZrO₃ layer at the interface between the zirconia (YSZ) electrolyte and the lanthanum strontium cobalt ferrite (LSCF) air electrode.⁷

Therefore, the reduction of the sintering temperature may present a solution to these challenges, in addition to a possible reduction of costs. Flash sintering is an advanced sintering technology aiming at reducing sintering temperature and time. It consists of the application of an electric field between two electrodes in contact with the green body, leading to a flow of current through the specimen to be sintered. The process is typically divided into three distinct stages: Stage I (incubation), where the current increases very slowly either with the increase of voltage or temperature; Stage II (flash event), in which a sharp nonlinear increase of conductivity causes the abrupt increase of current and drop of voltage; and Stage III (steady state), when the current density is stabilized at a constant value and the power source is switched from voltage to current control.8

As shown in the recent review of Wu et al.9 flash sintering has been successfully applied for the densification of typical SOCs electrolyte materials like YSZ and GDC, but also for alternative electrolyte materials like $BaZr_{0.1}Ce_{0.7}Y_{0.1}Yb_{0.1}O_3$. Additionally, it has been

investigated for proton-conducting electrolytes too, like La_{0.8}Sr_{0.2}Ga_{0.8}Mg_{0.2}O₃.¹¹ Zirconia is the most analyzed material, already introduced in the first articles of Cologna et al. from Prof. Raj's group, which focused on flash sintering of 3YSZ¹² and 8YSZ.¹³ After that, in Francis et al.,14 alternating layers of the fuel electrode (NiO and YSZ) and the electrolyte (YSZ) were successfully flash sintered. It was observed that the flash-sintered sandwich structure did not show delamination, contrary to the conventionally sintered (CS) samples, which suffered from the usual problems related to constrained sintering, such as delamination, cracking, or trapping of pores. Therefore, the potential of this process for multilayer samples was demonstrated at this early stage of development.

In this work, we focus on 10 mol% gadolinium-doped ceria (GDC10) building on previous works done in our group, where GDC10 dog bones were successfully flash sintered, as reported by Mishra et al. 15,16

GDC is a standard material in SOCs and has a broad range of potential applications, due to its favorable properties.^{17,18} In SOCs, it is commonly used as a dense barrier layer to avoid the SrZrO3 formation between the state-of-the-art YSZ electrolyte and LSCF air electrode.⁷ Although its ionic conductivity is higher than that of 8YSZ, 19 its chemical stability is lower, suffering from an extensive chemical expansion in reducing conditions.²⁰ Thus, its application as a dense electrolyte is challenging. Nevertheless, it can still be used instead of YSZ in the porous nickel-containing cermet fuel electrode (Ni-YSZ). In fact, thanks to the higher ionic conductivity, Ni-GDC electrodes show higher performance. 21,22 In addition, the low pO2 conditions at the fuel side transform GDC into a mixed-ionic-electronic conductor (MIEC),²¹ further increasing the reaction sites for electrochemical reactions. Few works in literature have shown the potential use of GDC as a single-phase porous electrode, as reported in Nenning et al.²³ and two works of Uecker and co-authors.^{24,25}

Therefore, GDC sintering is interesting from different microstructural perspectives: more porous for electrode applications or dense as an electrolyte. Its densification was also investigated by adding sintering aids, like Co₃O₄ or CuO, which decreased its sintering temperature, but on the other hand, caused a degradation of the electrochemical performance.^{26,27} Instead, a decrease of the sintering temperature can also be achieved by advanced sintering technologies, while simultaneously limiting the risk of performance degradation.

Mishra and coworkers have extensively investigated field-assisted and especially flash sintering of GDC10, the latter in the usual dog bone geometry. The processing map in Mishra et al. 16 shows the conditions for safe flash sintering: to reliably avoid crack formation, the electric field

conditions) on Wiley Online Library for rules of use; OA articles are governed by the applicable Creative Commons License

Iournal | 3 of 19

had to be limited to 250-300 V cm⁻¹ and the current density up to 100 mA mm⁻². The current localization coupled with hot spot formation was prevented by limiting the current density below 250 mA mm⁻², but with a field strength not exceeding 90 V cm⁻¹. The latter combination of parameters, with a furnace temperature of 680°C, is suggested as optimal for the full and safe densification of GDC10. Still, these samples presented inhomogeneous microstructure, with abnormal grain growth at the positive electrode (anode) and closed porosity paired with by small grain sizes at the negative electrode (cathode). This was due to the opposite gradients of oxygen vacancies and oxygen ions, migrating toward the cathode and toward the anode, respectively. Flash sintering can be optimized if carried out in current-rate control mode, as first reported by Kumar et al.²⁸ and also shown in Mishra et al.¹⁵ With this method, the typical power surge at the flash onset is prevented, therefore, avoiding electrode overheating.

Other results on flash sintering of GDC bulk samples are presented in literature: Hao et al.²⁹ densified GDC20 in a few seconds at 545°C and with a field strength of 20 V cm⁻¹, values lower than the typical ones for zirconia. However, the specific power dissipation critical to initiate the flash was 10 mW mm⁻³, which matches the range of 8YSZ.³⁰ Valdebenito et al.³¹ needed a higher field strength of 100 V cm^{−1} to initiate flash sintering of GDC10, attributing the discrepancy with GDC20 to the initial different oxygen vacancy concentration. However, the specific power dissipation was in the range of 20-30 mW mm⁻³, following the typical range of 10-50 mW mm⁻³ observed for most of oxide ceramics.³⁰ A more extended study from Spiridigliozzi et al.³² compared different concentrations of gadolinium, that is, GDC5, GDC10, GDC15, and GDC20, showing that an increasing amount of gadolinium caused a reduction of the flash onset temperature, but the biggest difference was noticed between GDC5 and GDC10. The results are aligned with the other works: GDC10 could be fully sintered with a field strength of 100 V cm⁻¹ at a furnace temperature just below 600°C.

However, all these results report on bulk samples (dog bones, pellets, cylinders) but the application of flash sintering for thin functional layers is still in a relatively early stage of development and detailed reports in literature are rare.

For this reason, we present here a novel study to show the feasibility of flash sintering on GDC10 thin layers, with a green layer thickness below 10 $\mu m-a$ realistic value in the context of SOC components. A specific challenge was the densification of a green layer onto a rigid substrate, leading to a strong degree of constrained sintering. Thus, we modified the setup from Guillon et al. 33 used for investigating constrained sintering of alumina thin layers. However, the proposed in-situ shrinkage measurement

TABLE 1 Powder particle size distribution and specific surface area

GDC10 Treibacher	D ₁₀ (μm)	D ₅₀ (μm)	D ₉₀ (μm)
Before sonication	8	25	50
After sonication in ethanol	0.05	0.3	20.5
Specific surface area		$7 \ m^2 \ g^{-1}$	

using a rocking arm and a high-precision laser was not reliable enough under the application of a high electric field. Therefore, we had to limit the investigation of the sintering behavior to ex-situ analyses of the flash-sintered layers with respect to microstructure, thickness, and electrical conductivity.

As detailed in the results, the required parameters to achieve flash conditions and visible effects of the current appear to be much harsher than the usual parameters reported in the literature for GDC10 bulk samples. The special specimen geometry and the unusual experimental setup play an important role in that regard.

2 | MATERIALS AND EXPERIMENTAL METHODS

2.1 | Powder and screen-printing paste

The starting material was a commercial 10 mol% gadolinium-doped ceria (GDC10) powder from Treibacher (lot n. EA35/12.1) and its particle size distribution was determined, before and after 3 min of sonication in ethanol, with a laser diffraction Horiba LA-950 analyzer. The specific surface area was measured by nitrogen adsorption (Area Meter II, Juwe Laborgeräte GmbH). Table 1 displays the results of the two measurements.

Additionally, Scanning Electron Microscopy (SEM) was used to characterize the powder. Figure 1A,B shows that the powder consists of coarse spherical agglomerates of about 20 μ m containing primary particles smaller than 1 μ m. The results of Table 1 suggest that these agglomerates are soft enough to be broken by sonication.

The screen-printing paste was obtained by mixing 65.4 wt% of presuspension and 34.6 wt% of transport suspension. The presuspension was prepared into a PET bottle with: 79 wt% of GDC10 powder, 1.26 wt% of dispersant Nuosperse FX9086 (Elementis Specialties, Inc.), 19.74 wt% of anhydrous terpineol solvent (Sigma–Aldrich). Zirconia milling balls with diameters of 5 and 10 mm in ratio 1:1 were added to fill the bottle up to 2/3 of the total volume and the presuspension was then mixed in a tumbler mixer for 48 h at 67 rpm. The transport suspension was prepared in a hot mineral oil bath at 70°C by mixing the 85 wt% of solvent (terpineol, Sigma–Aldrich) and the 15 wt% of binder, that

15512916, 2025, 10, Downl

com/doi/10.1111/jace.70033 by Forschungszentrum Jülich GmbH Research Center, Wiley Online Library on [20/08/2025]. See the Terms

) on Wiley Online Library for rules of use; OA articles are governed by the applicable Creative Commons Licens

FIGURE 1 (A, B) SEM images of the starting GDC10 powder.

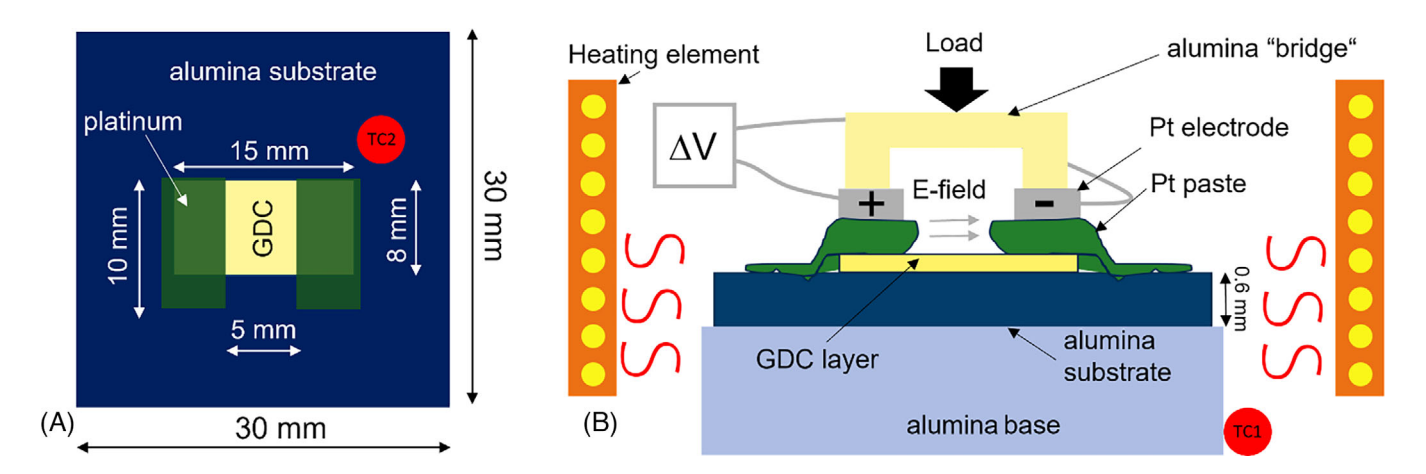


FIGURE 2 (A) Scheme of the specimen; (B) experiment assembly.

is, an ethyl cellulose powder (45 cP, medium chain length, Sigma–Aldrich).

For screen printing, an EKRA E2 semi-automatic machine was used: the GDC10 paste was pushed through a screen with an open area of 39%, mesh width 115 μ m, wire diameter 64 μ m, and theoretical wet layer thickness 40 μ m. The rubber squeegee was moved at 100 mm s⁻¹ with a constant pressure of 1.5 bar and a snap-off distance between the screen and the alumina substrate of 1.5 mm. After printing, the paste was let dry for 1 h at 60°C in air, but no presintering was carried out.

2.2 | Flash sintering

Figure 2A shows the sketch of the specimen, where the GDC10 layer, in yellow, is screen printed onto a $30 \times 30 \text{ mm}^2$ and $600 \, \mu \text{m}$ thick alumina dense substrate (CeramTech). This material, being a very high electrical insulator, guaranteed that the electric current could flow through the GDC10 layer only. In addition, the substrate had to be tough enough to withstand a certain load, as explained later.

The electric contact for flash sintering was ensured by screen-printing two platinum stripes (in green in Figure 2A) on the GDC10 layer, with a 5 mm gap between them. The high-purity Pt paste (Heraeus) was slightly diluted with 5 wt% terpineol to facilitate the screenprinting, after that, drying took place overnight at room temperature. Two flat Pt electrodes were contacted to the Pt stripes and held in place by an alumina "bridge" pushed by the Instron load cell with 10 N force. This load was the minimum value provided by the Instron load cell and proved to be enough to keep the electrodes firmly in place for the entire experiment. Figure 2B shows the scheme of the experiment. The details of the setup, namely, a sinterforging furnace, are described in the first report of Aulbach et al.34 After operating with cylindrical samples, this furnace was adopted for the study on constrained layers by Guillon et al.³³ More recently, the setup was modified to operate with an electric field, but still with cylindrical samples, as in the works of Cao et al.35 and Dash et al.36 A very similar experiment setup is also reported by Francis and Raj.³⁷ In the present work, the setup was further modified enabling to apply the electric field to thin layers. The load transferred by the alumina bridge ensured good

Journal 1

electric contact. Furthermore, a more accurate power source than that in the former works was used (Sorensen DLM 300-2) guaranteeing a better parameter control, despite the disadvantage of operating in DC voltage only.

The electric field was applied in the layer plane and the Instron push rod maintained constant contact against the alumina bridge along the entire experiment (Figure 2B). Given the electrode gap being 0.5 cm, the absolute value of the applied voltage, in V, is half of the electric field (V cm⁻¹). In the results, the values are given only in the unit of an electric field.

All flash sintering experiments were carried out under isothermal conditions in voltage-to-current control mode, similarly to the work of Francis and Raj. 38 The DC voltage was either applied as a step function or manually increased, depending on the case. All the specimens were heated to the maximum temperature (usually 1200°C, heating/cooling rates 15°C/min) and held under a constant electric current for a certain dwell time. One thermocouple (TC1) regulated the furnace temperature and was placed beside the alumina support (Figure 2B, alumina in light blue, TC1 in red), at 40 mm from the heating elements. The second thermocouple (TC2) was put in direct contact with the specimen, onto the alumina substrate, at about 3 mm from the GDC10 layer (Figure 2A). The system was let to equilibrate for 10 min before applying the voltage and TC2 was used as the reference temperature.

The operation range of the power source was 0-300 V for the voltage and 0-2 A for the current. The voltage, the current, the furnace, and the sample temperatures were recorded together with LabVIEW.

Four sets of flash sintering experiments were conducted, as reported in Table 2. In Set I, the same specimen A was subjected to several flash sintering cycles to screen the optimal range of parameters for the following experiments. In particular, the effect of temperature and electric field was investigated in relation to the incubation time. In Set II, the current density was the parameter in analysis, with a different specimen (B, C, D, E) for each sintering experiment. Set III (specimens F, G, H, I) aimed at the variation of the dwell time, keeping the other parameters constant. Two independent and single experiments were carried out in Set IV, for specimens J and K, respectively. Specimen Kcond. was used for the electric conductivity measurements after flash sintering, as detailed in the next section. Specimen J-vert. was mounted in a special vertical configuration to directly observe the flash phenomenon. As shown in Figure 3A, it was hanged in a vertical position fixed by two platinum wires coiled around two holes, allowing a direct observation through a vertical hole of the furnace. The platinum paste was brushed to extend the electric contact from the wires to form two electrodes on top of the GDC10 layer. Figures 3B and C display the specimen photos in the

furnace at 1200°C, without and with electric current (100 mA), respectively. Taking advantage of the vertical position, the thermocouple TC2 could be placed against the backside of the alumina substrate, corresponding to the GDC10 layer (Figure 3A). This allowed the measurement of the sample temperature in a closer position than the rest of the other experiments. The furnace temperature was measured as usual by the TC1 (Figure 2B).

Characterization 2.3

A white light Topograph Cyber-scan CT350T (cyberTECH-NOLOGIES GmbH) with a chromatic sensor CHR1000 was used for optical analyses. The thickness and roughness of the as-screen-printed layers was measured, ensuring a good homogeneity and reproducibility of the process. Additionally, the layers were also analyzed after flash sintering, but due to the small defects/deformations, the analysis was only qualitative. The thickness was then measured only on polished cross sections by SEM (Zeiss Gemini Ultra 55, Carl Zeiss NTS GmbH). Furthermore, the 2D porosity area was determined with the software ImageJ by simply calculating the percentage area of the pores.

We tried to measure the shrinkage in-situ with a cantilever using the method proposed in Guillon et al.,³³ but the measurement failed due to the interaction of the laser signal with the high electric field. For the sake of completeness, one exemplary measurement is reported in the Supplementary Information (Figure S1).

The in-plane electric conductivity of two samples was measured, both sintered for 3 h, one with (specimen Kcond.) and one without an electric field. The impedance measurements were carried out in a custom-built 4-point electrochemical contact station for high-temperature conductivity measurements (Huber Scientific). Both the Pt stripes (i.e., electrodes) were contacted by Pt/Ir needles and measured simultaneously in the same furnace under identical conditions (2-point measurements for two samples). Electrochemical impedance spectroscopy measurements were carried out using an impedance analyzer (Alpha-20 A High-Performance Frequency Analyzer, Novocontrol Technologies GmbH & Co.KG) at temperatures between 400 and 800°C. The temperature was first increased in a stepwise manner before it was decreased again. The first measurement was taken under oxidizing conditions using synthetic air (21% O₂ in N₂, 99.999% purity, Messer). After that, another measurement was performed using the same temperature program but under slightly reducing conditions using humidified hydrogen with an H₂O:H₂ ratio of roughly 1:1 (humidified Inoxline, \sim 23 mbar H₂O + 2% H₂ in Ar, Messer).

TABLE 2 Flash sintering experiments with parameters and observations.

TABLE 2 Flash sintering experiments with parameters and observations.								
Set	Sample	Temperature (furnace) [°C]	Initial current density ^a [mA mm ⁻²]	Final current density ^b [mA mm ⁻²]	E-field max. value [V cm ⁻¹]	Incubation	Dwell time [min]	Observations
Set I	A-600	1200	≈800	-	554	1	-	Set 600 V cm ⁻¹ , fast current response
	A-500	1200	≈800	-	500	45	-	Fast current response
	A-450	1200	≈800	-	450	90	-	No E-field drop
	A-400	1200	≈700	-	400	430	-	E-field too low, long incubation time
	A-1100-600	1100	≈800	-	600	35	-	Fast current response
	A-1100-500	1100	≈650	_	500	290	-	Low E-field and/or T, long incubation
	A-1050-600	1050	≈770	-	600	370	-	Low T, long incubation
	A-500/2	1200	≈800	-	500	1	-	Faster current response than A-500
	A-400/2	1200	≈800	-	400	220	-	No E-field drop, but shorter incubation than A-400
Set II	B-0	1200	0	0	0	-	240	None
	C-150	1200	≈155	≈190	160	180	240	Slow E-field drop to 120 V $\rm cm^{-1}$
	D-300	1200	≈310	≈380	300	120	240	Slow E-field drop to 270 V ${\rm cm}^{-1}$
	E-600	1200	≈620	≈910	400	150	240	Fast E-field drop to 300 V ${\rm cm^{-1}}$
Set III	F-180-0	1200	0	0	0	-	180	None
	G-45	1200	≈800	≈1190	500	600	45	Fast E-field drop to 400 V ${\rm cm^{-1}}$
	H-90	1200	≈800	≈1250	520	180	90	Fast E-field drop to 400 V ${\rm cm}^{-1}$
	I-180	1200	≈800	≈1310	530	300	180	E-field drop as H-90
Set IV	J-vert.	1200	≈up to 1600	-	_	-	varied	Electroluminescence and Joule heating
	K-cond.	1200	≈1600–800	_	530	-	180	Shortly at higher current density (1600 mA mm $^{-2}$), then 3 h at 800 mA mm $^{-2}$

Note: Set I: Adjusting the optimum range of flash sintering parameters (electric field and temperature). Set II: Systematic variation of current density. Set III: Systematic variation of dwell time. Set IV: Specific setups for temperature control and electrochemical tests.

 $^{^{\}mathrm{b}}$ The final current density is calculated from the final thickness reported in the SEM images (Figures 7 and 8).

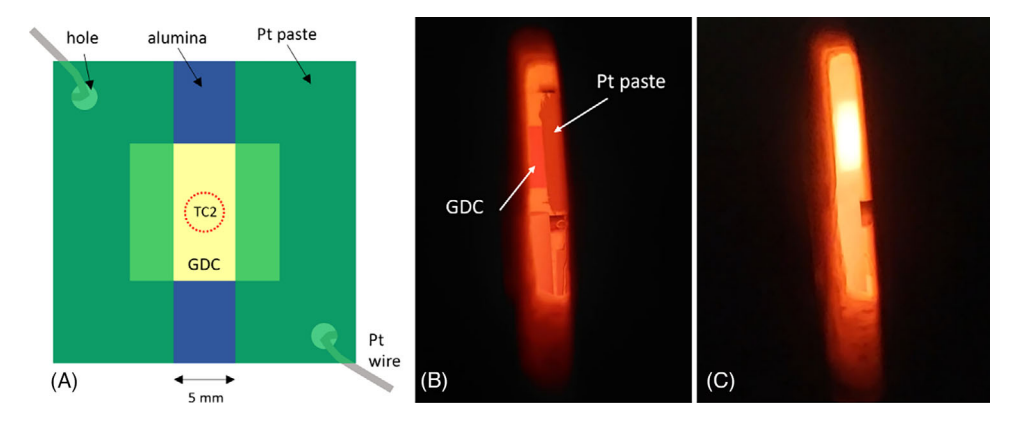


FIGURE 3 Experimental setup for specimen J-vert. (A) Sketch of the specimen in a vertical position. TC2 is placed on the back side, in contact with the alumina substrate. (B) Specimen photo in the furnace at 1200°C. (C) Application of electric current (100 mA) and electroluminescence of the GDC10 layer (furnace at 1200°C).

^aThe initial current density is calculated from the green layer thickness: 7.5 μm for samples A, and F to I; 9 μm for B to E.

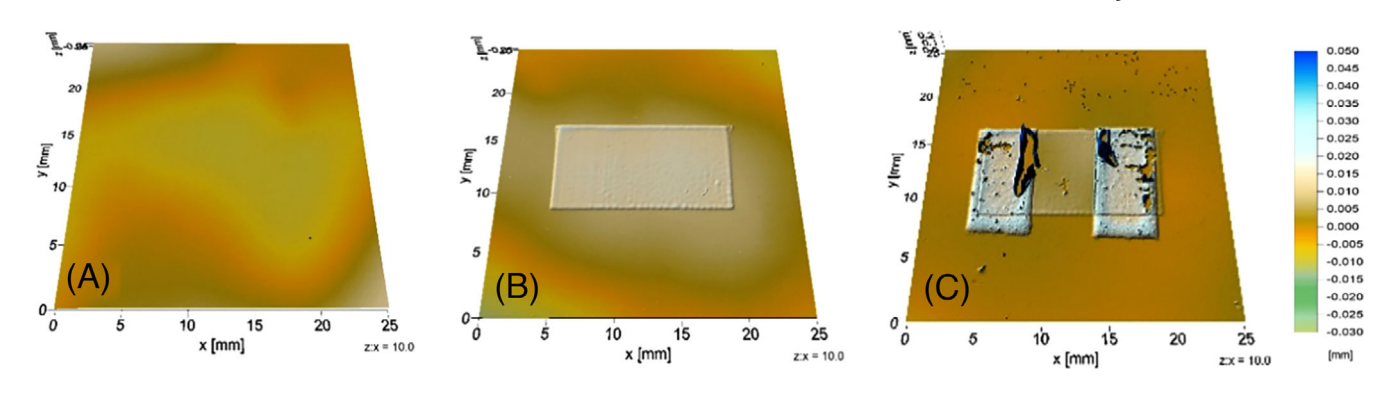


FIGURE 4 White light topography, in (A) the alumina substrate, in (B) with the GDC10 layer after screen printing, in (C) with the Pt stripes and after flash sintering.

3 | RESULTS

Figure 4A–C shows one example of the Cyber-scan optical analyses used to evaluate the quality of the screen-printed layers before and after flash sintering: (a) measurement of the substrate as reference; (b) GDC10 layer after screen-printing; (c) GDC10 layer and Pt stripes after flash sintering. These measurements had the primary scope of ensuring a good reproducibility of the screen-printing process. The average roughness (root mean square) of 12 GDC10 green layers resulted in $R_q = 0.21~\mu m$ and an average thickness of 7.5 μm . Thus, the initial layer cross-section, used for the calculation of the initial current density, was $8\times0.0075~mm^2$.

The green layer thickness of specimens B, C, D, and E was determined only by SEM analysis, giving an average value of 9 μ m (Figure 7A,B). These samples were screen printed as a separate batch, where the layer dimension was 15 \times 15 mm², therefore, the initial cross-section was \sim 15 \times 0.009 mm². The thickness of the sintered layers was exclusively measured by SEM analysis because small damages and defects occurred during sintering impeding an accurate measurement by the Cyber-scan (Figure 4C represents a very good layer, but the average quality was a bit lower).

Table 2 summarizes all the experiments conducted with the flash sintering setup, including those reference specimens sintered without electric current. The temperature reported refers to the furnace temperature. The initial current density is calculated from the green layer thickness, while the final (maximum) current density refers to the final cross-section observed in the SEM analyses. The green layer thickness can be assumed as the initial thickness just before the application of current because the heating ramp up to the maximum temperature did not cause any significant densification. This can be observed in Figure S2, in the Supplementary Information, where the microstructure of an as-screen printed layer is com-

pared with a specimen heated at 1200°C and quenched by switching off the furnace. In the rest of the text, with "current density" is meant the value referred to the green layer thickness, that is, the initial current density, otherwise, it is specified as "final current density." The reported electric field indicates the maximum value, corresponding to the transition to the current-controlled regime. The numbers after the letter of each specimen (or test) indicate the main varying parameter and are shown in bold in Table 2.

The parameters were varied for each set with the following criteria:

- Set I: Specimen A underwent several flash sintering cycles with the threshold current density fixed at 800 mA mm⁻² (corresponding to set 48 mA). The temperature and the electric field were the varying parameters, while the incubation time was the output result.
- Set II: The choice of temperature for Set II was based on the results of Set I. The criterion was to minimize the incubation time, so as to reach the constant current stage in the shortest time (stage III of flash sintering) and investigate only the effect of current density.
- Set III: The current density for Set III was chosen based on what was observed in Set II. The effect of time was then investigated at a constant current density.

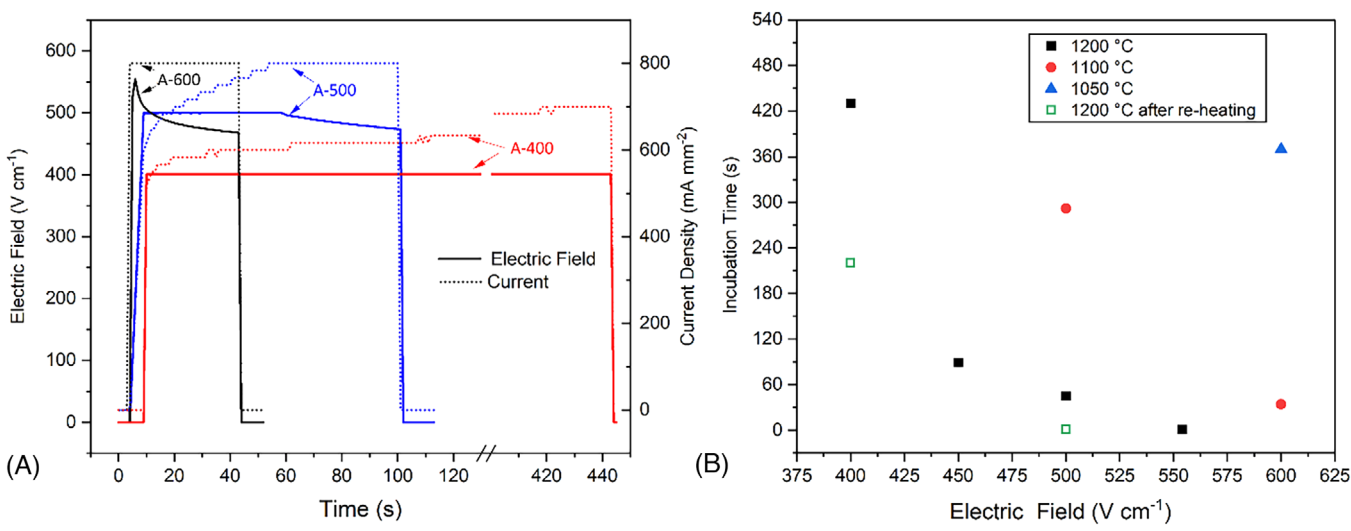
Set I started with the first test at 1200°C, a temperature relatively lower than the GDC conventional sintering around 1400°C.³⁹ The variation of the other parameters can be seen in detail in Table 2.

The applied electric field and furnace temperature were progressively decreased and the relative incubation time was calculated. Figure 5A shows for the sake of simplicity only three tests of Set I: A-600, A-500, and A-400, carried out at 1200° C with a set electric field between 600, 500, and 400 V cm^{-1} , respectively. Figure 5B reports the incubation times for all the experiments of Set I. In Figure 5A, it can be observed that the transition to the current-controlled

15512916, 2025, 10, Down

Jülich GmbH Research Center, Wiley Online Library on [20/08/2025]. See the Terms

on Wiley Online Library for rules of use; OA articles are governed by the applicable Creative Commons Licens



Set I experiments: (A) different set electric fields at 600, 500, and 400 V cm⁻¹. (B) Incubation time as a function of the set electric field and temperature. All the data points correspond to Set I of Table 2.

regime occurs instantaneously for A-600, so quickly that the actual electric field reaches only 554 V cm⁻¹. This transition is usually marked by a sudden drop, indicating an increase in conductivity typical of the flash sintering regime (Stage II of flash). As expected, a decrease in either the applied electric field or furnace temperature results in a longer incubation time (Figure 5B). When the furnace temperature is reincreased to 1200°C again, the incubation time is shorter than in the initial state (A-500/2 and A-400/2). This is likely due to the multiple sintering cycles undergone by the same specimen, which increased both conductivity^{40,41} and microstructure density. The power supply, being limited to 300 V, prevented to explore the combination of higher electric fields than 600 V cm⁻¹ at lower temperatures. However, the trend in Figure 5B is consistent with the findings of Francis and Rai, 38 who concluded that the electric field serves as the thermodynamic driving force for the flash effect.

If the electric field and/or the temperature are too low, the current density threshold cannot be reached, even waiting for a long time (long incubation). This is, for example, the case of A-400 and A-1100-500. A fresh sample under the same conditions would show an even longer incubation time, because of the lower conductivity and density, which means these conditions are not guaranteeing a typical sudden conductivity increase, which is characteristic of flash sintering.

In conclusion, for Set II, 1200°C was chosen as the optimal furnace temperature to ensure a sufficient increase in conductivity. The electric field was manually increased to flash the specimens at different threshold current densities. Specimen B-0 served as a reference and was sintered at 1200°C for 4 h without electric current. The preset current density threshold was doubled each time for specimens C-150, D-300, and E-600 from 155, to 310, to 620 mA mm⁻²,

respectively. To allow a direct comparison with the conventional sintering, the dwell time was also 4 h, at 1200°C. Figure 6A shows the trend of their electrical parameters over time. The incubation time was recorded, but its significance is limited as it also depended on the voltage increase rate. In Figure 6A, the solid black curve for specimen E-600 shows an abrupt drop of electric field, corresponding to a sudden conductivity increase. Specimens C-150 and D-300, instead, seem to have a softer transition to the currentcontrolled, not fully matching the dynamic of the flash regime.

For Set III (specimens F-I), focusing on the effect of the dwell time, the temperature was fixed at 1200°C and the threshold current density at 800 mA mm⁻², similarly to Set I. This current density was well above than that of E-600, ensuring in this way a sudden conductivity increase, typical of flash sintering. Figure 6B displays the voltage and current curves for the specimens G-45, H-90, and I-180, flashed at constant current density for 45, 90, and 180 min, respectively.

Figures 7A-J and 8A-J present the SEM cross-sections of the second and third series from Table 2, respectively. Each specimen is presented at two different magnifications, but actually, several acquisitions in different spots displayed a rather good homogeneity. However, the analysis focuses on the layer area not covered by the Pt paste, as this region typically shows a denser microstructure due to applied pressure from the Instron load cell and likely lower heat dissipation (see Supplementary Information, Figure S3).

Figure 7A,B displays a pristine GDC10 layer after screenprinting with a thickness of about 9 µm. Delamination from the substrate is likely due to sample preparation, as no thermal treatment was performed. The effect of current density is only partially visible when comparing

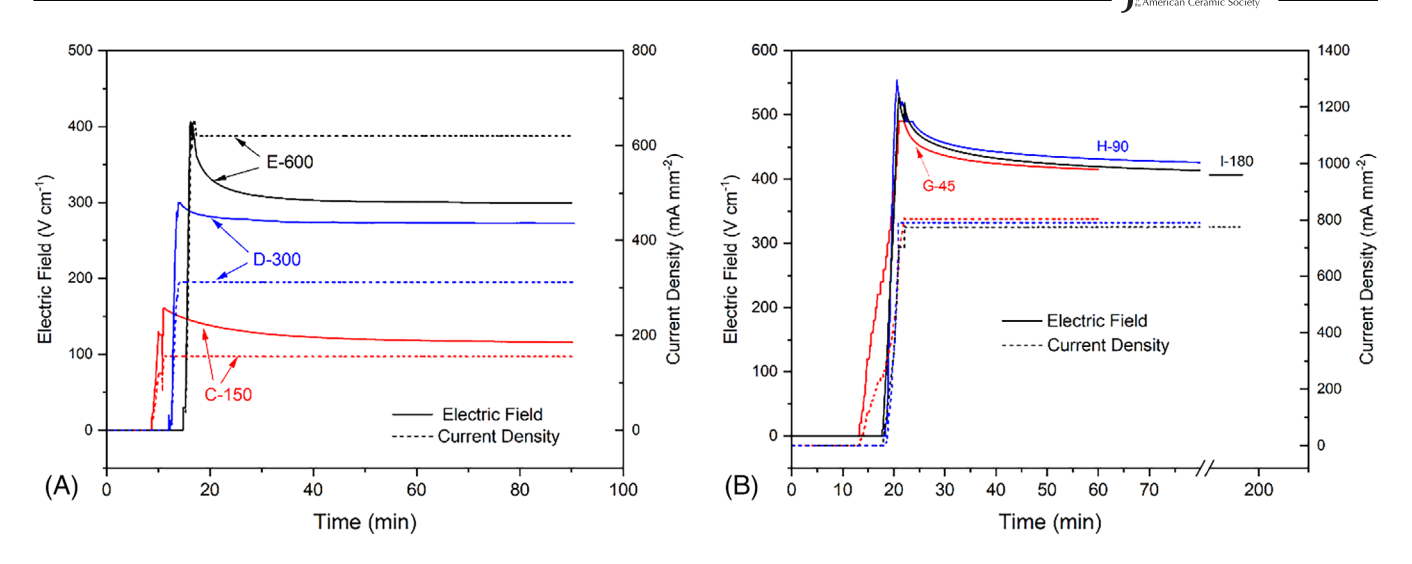


FIGURE 6 (A) Set II with current density thresholds at 150, 300, and 600 mA mm⁻². (B) Set III with different dwell times between 45, 90, and 180 min, at a constant current density of 800 mA mm⁻².

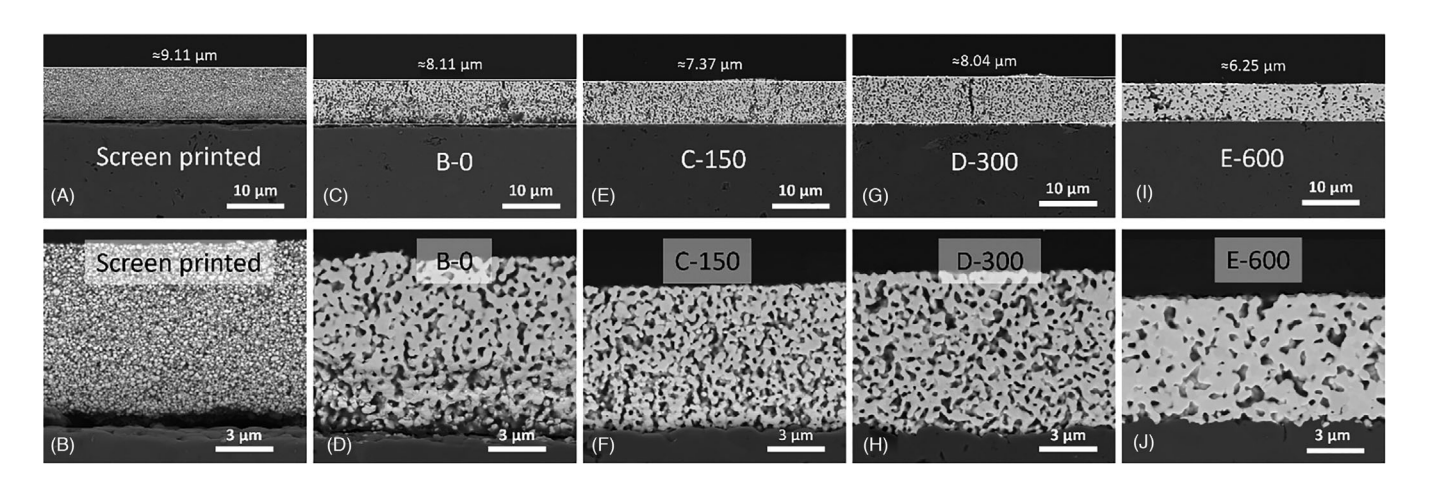


FIGURE 7 (A, B) GDC10 green layer; (C, D) specimen B-0 sintered without electric current, at 1200°C for 4 h; (E, F) sample C-150 sintered with electric current (150 mA mm⁻²), at 1200°C for 4 h; (G, H) sample D-300 sintered with electric current (300 mA mm⁻²), at 1200°C for 4 h; (I, J) sample E-600 sintered with electric current (600 mA mm⁻²), at 1200°C for 4 h.

≈6.40 µm	≈5.36 µm	≈5.00 µm	≈4.67 μm	≈4.60µm
F-180-0	G-45	H-90	I-180	CS 1400°C
(A)	(C) 10 µm	(E)	(G) <u>10 μm</u>	(l) 180 min ^{10 μm}
	(a) (b)			
F-180-0	G-45	H-90	I-180	CS 1400°C
(В) <u>^{3 µт}</u>	(D) <u>3 μπ</u>	(F) <u>з µт</u>	(H) <u>з µт</u>	(J) 180 min <u>3 μm</u>

FIGURE 8 (A, B) sample F-180, sintered without electric current at 1200° C, 180 min; (C, D) sample G-45 sintered at 1200° C, with 800 mA mm⁻², 45 min; (E, F) sample H-90 sintered at 1200° C, with 800 mA mm⁻², 90 min; (G, H) sample I-180 sintered at 1200° C, with 800 mA mm⁻², 180 min; (I, J) sample conventionally sintered at 1400° C, 180 min.

15512916, 2025, 10, Downloaded from https

onlinelibrary.wiley.com/doi/10.11111/jace.70033 by Forschung

Jülich GmbH Research Center, Wiley Online Library on [20/08/2025]. See the Terms and Conditions (https://onlinelibrary.wiley

on Wiley Online Library for rules of use; OA articles are governed by the applicable Creative Commons License

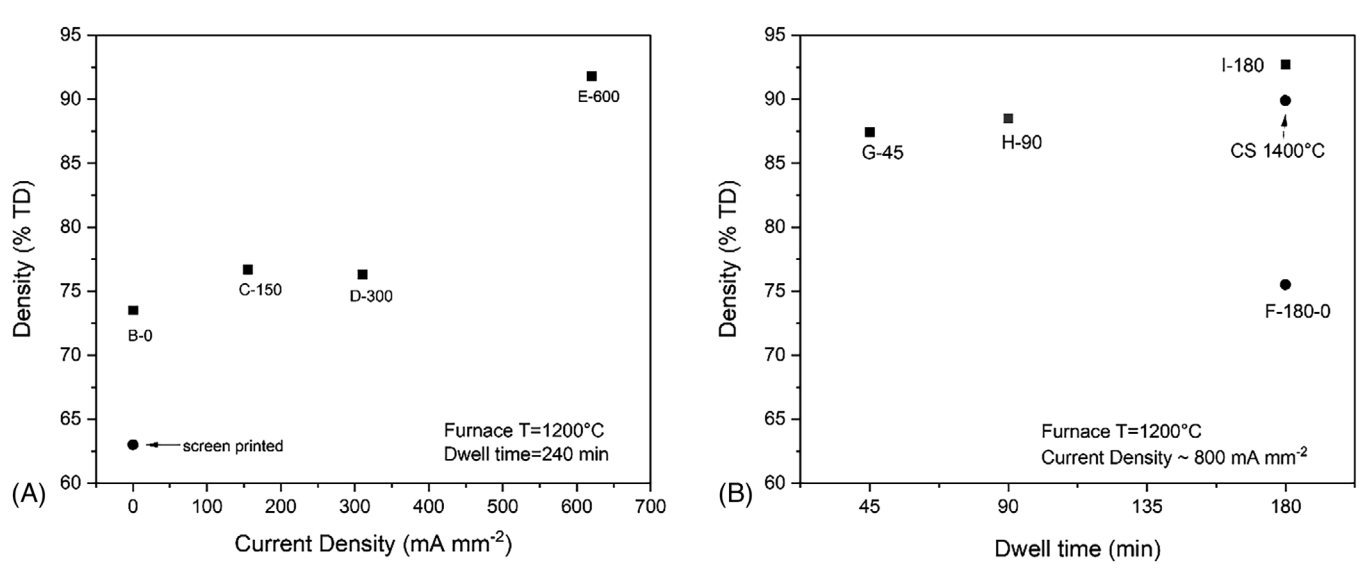


FIGURE 9 Densities dependency on the current density (A), and on the dwell time (B).

specimens C-150 and D-300 to the reference B-0. Interestingly, the layer thickness for D-300 is slightly higher than C-150, contrary to expectations. A noticeable change occurs only for E-600, where the layer thickness decreases significantly to approximately 6.25 µm and the microstructure appears much denser (Figure 7J). As seen in Figure 6A, the minimum current density for E-600, around 620 mA mm⁻², appears to be a clear minimal threshold for densification. Additionally, due to layer shrinkage, the final current density reaches approximately 910 mA mm⁻².

Besides the Set III specimens, Figure 8 also displays the microstructure of a CS specimen at 1400°C for 3 h (Figure 8I,J). This batch of specimens belong to those previously analyzed by the Cyber-scan, whose green layer thickness resulted in 7.5 µm. The effect of electric current on densification is evident when comparing specimen F-180-0, sintered without current for 3 h, to specimen G-45, flash sintered for 45 min. The initial current density for G-45 is $\sim 800 \text{ mA mm}^{-2}$, increasing to 1190 mA mm⁻² by the end of the heat cycle. As with conventional sintering, increasing the dwell time for specimens H-90 and I-180 results in higher density and thinner layers. Longer dwell times promote densification, leading to higher current densities that further enhance the process. This suggests that while high current densities play a key role, the effect of time remains significant as well, with densification reaching saturation on a longer timescale. Interestingly, the conventional sintering at 1400°C for 3 h (Figure 8J) results in a layer thickness similar to that of specimen I-180, but with a microstructure featuring slightly larger pores.

The density of the samples in Figures 7 and 8 was estimated by image analysis, determining the porous area of the SEM cross-sections. Figure 9A,B displays the density as

a function of the set current and dwell time, respectively.

Figure 10A,B presents the results of experiment J-vert. from Figure 3, showing the temperatures from thermocouples TC1 and TC2 as functions of time, alongside current density and electric field. In Figure 10A, the electric field increases to 400 V cm⁻¹ and remains constant for 7 min, while the current rises without a set threshold. The experiment ends when the electric field is turned off, and the current density reaches 400 mA mm⁻². Initially, TC2, which is placed against the backside of the alumina substrate (Figure 3A), has a constant offset compared to TC1 (10°C). However, as the current increases, TC2's temperature follows the current's trend, while the electric field remains constant. By the end, the temperature difference between the two thermocouples is 28°C. Figure 10B shows the effect of the gradual increase of the current density threshold from 350 to 650 mA mm⁻² (maximum difference 34°C). At each step, TC2's temperature increases slightly, and when the current density drops to zero, TC2's temperature drops immediately too, reestablishing the initial temperature difference. Similarly, when the current density jumps from 0 to 650 mA mm⁻², TC2 responds accordingly. Although TC1 is also affected by current changes, the temperature shift is minimal. This experiment highlights the rapid temperature response to current changes and a Joule heating effect in the specimen. However, from the observations in-situ of Figure 3B,C, the alumina substrate never displayed the typical light emission of flash sintering, which was limited to the GDC layer only. This can also be deduced by the modest temperature increase in the alumina substrate.

The last sample in Table 2, K-cond., was flash sintered at 1600 mA mm⁻² for 12 min, then the current density was reduced to 800 mA mm⁻² and held for 3 h. Its Femperature (°C)

(A)

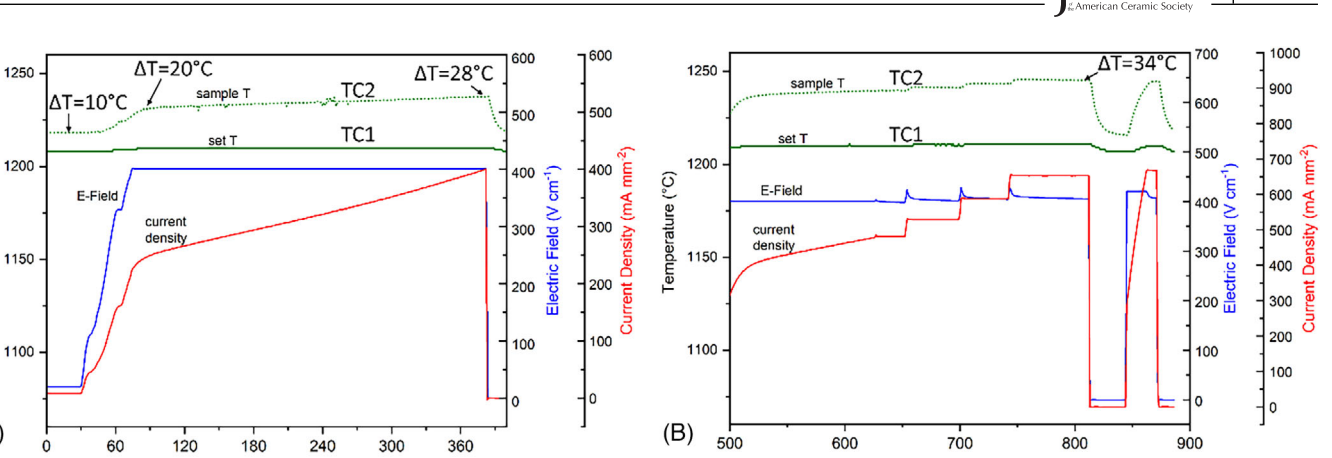


FIGURE 10 Flash sintering for specimen J-vert. in the configuration of Figure 3. The temperature of the two thermocouples TC is reported as related to the electrical parameters. (A) Experiment with a constant electric field. (B) Experiment with stepwise increase/decrease of current density.

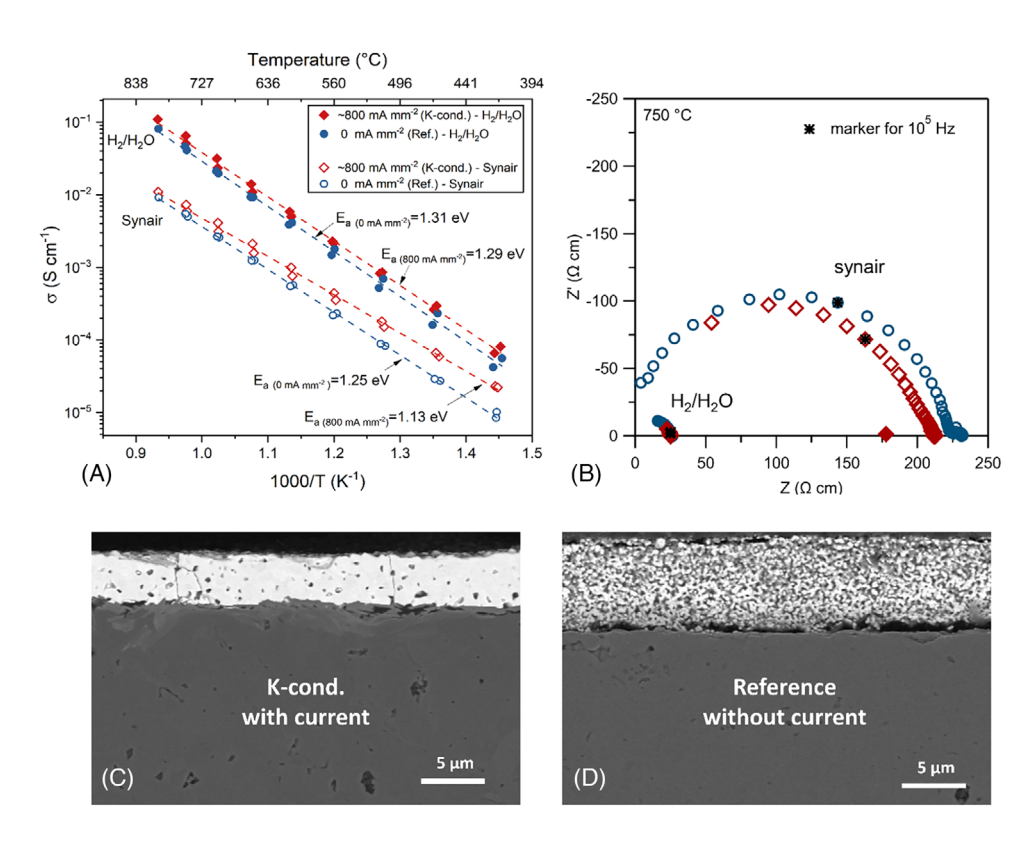


FIGURE 11 (A) Total conductivity as a function of the inverse temperature for two samples, sintered in the presence of current (diamonds) and conventionally (circles), and in H_2/H_2O (full symbols) or in synthetic air (empty symbols). (B) Exemplary Nyquist plots at 750°C. (C) SEM image of the sample K-cond. flash sintered for 12 min with 1600 mA mm⁻², then for 3 h with 800 mA mm⁻² (T = 1200°C). (D) SEM image of reference specimen conventionally sintered (0 mA) for 3 h at 1200°C.

in-plane electric conductivity was measured and compared to a sample sintered without an electric field, held at 1200°C for 3 h in air. Figure 11 reports the impedance measurements and their microstructure: in Figure 11A, the total conductivity is plotted as a function of the inverse temperature for two atmospheres. Figure 11B

Time (s)

presents exemplary Nyquist plots of the impedance measurements at 750°C using the same legend as in Figure 11A. Figures 11C and D show the microstructures of the flash-sintered (K-cond.) and CS samples, respectively. The microstructures differ significantly, with K-cond. exhibiting a substantial higher density. Nevertheless, the

Time (s)

15512916, 2025, 10, Downloaded from https://ceramics.onlinelibrary.wiley.com/doi/10.1111/jace.70033 by Forschungs entrum Jülich GmbH Research Center, Wiley Online Library on [20/08/2025]. See the Terms and Conditions (https://onlinelibrary.wiley) on Wiley Online Library for rules of use; OA articles are governed by the applicable Creative Commons License

electrical conductivity results comparable between the two specimens.

The conductance/resistance is normalized to the sample geometry. The conductivity σ is calculated according to Equation (1):

$$\sigma = \frac{1}{R} \cdot \frac{A}{d},\tag{1}$$

where R is the measured resistance at the low-frequency x-axis intercept in the Nyquist plot, A is the correctional area of the sample, and d is the distance between the two Pt electrodes of each specimen.

Due to the geometry of the measurement setup, the semi-circle arc in the Nyquist plot results from the setup capacitance ($\sim 10^{-12}$ F), which is orders of magnitude larger than the grain and grain-boundary capacitances of the GDC layer ($\sim 10^{-15}$ F). Therefore, the bulk total resistance of GDC is extracted using the low-frequency x-axis intercept. The electrode features from the Pt electrodes are not visible in this case, since the ohmic (bulk) resistance of GDC is orders of magnitudes higher than the oxygen exchange resistance for this geometry.⁴² In H_2/H_2O , the conductivity of both samples is similar, but due to the more reducing conditions, it is about an order of magnitude higher than in synthetic air. Possible reasons for this increase in conductivity are an increase in electronic conductivity caused by a higher Ce³⁺ concentration under reducing conditions, making GDC an MIEC, or a decrease in grain-boundary resistance.⁴³ Under synthetic air, the conductivities are also comparable, except for the lowest temperatures, where the conductivity of specimen K-cond. is higher, but still in the same order of magnitude. Figure 11A also displays the values of the activation energies (Ea) for each measurement, determined from the slope of the $ln(\sigma T)$ versus T^{-1} . The values range from 1.13 to 1.31 eV.

4 | DISCUSSION

4.1 | Background

To the best of our knowledge, this is the first study reporting the application of flash sintering to thin layers produced using an industrial-like process as screen-printing. The motivation for this investigation stems from previous research conducted by our group. On one hand, Mishra et al. explored flash sintering of GDC10 dog bones. ^{15,16} On the other hand, Cao et al. ^{35,44} investigated discontinuous sinter-forging on yttria-stabilized ceria cylinders. They found that under isothermal conditions and in the presence of an electric field, the uniaxial viscosity decreased,

while the viscous Poisson's ratio (ν^p) increased. This is relevant to constrained sintering, as ν^p influences the densification rate of a porous film on a rigid substrate. According to Green et al.,⁶ the relationship is given in Equation (2):

$$\dot{\varepsilon}_{z}^{constr.} = \frac{1 + \nu^{p}}{1 - \nu^{p}} \dot{\varepsilon}^{free}, \tag{2}$$

where $\dot{\varepsilon}_z$ is the strain rate in the direction of the film thickness and $\dot{\varepsilon}^{free}$ is the free sintering strain rate of the unconstrained film. Since the volumetric densification rate for the unconstrained film is $3\dot{\varepsilon}^{free}$ in the case of isotropic behavior, the normalized volumetric densification rate of the constrained film is given in Equation (3)^{45,46}:

$$\left(\frac{\dot{\rho}}{\rho}\right)^{constr.} = \frac{1 + \nu^p}{3(1 - \nu^p)} \left(\frac{\dot{\rho}}{\rho}\right)^{free}.$$
 (3)

For porous bodies, where $v^p < 0.5$, this suggests that the densification rate of the constrained layer is lower than that of the free layer. In the absence of an electric field, in principle, v^p does not depend on temperature, but only on microstructure (i.e., density). However, under an electric field, an increase in v^p is expected to occur and mitigate the constraint, facilitating densification. Cao et al.^{35,44} demonstrated this effect under low electric fields (14 and 28 V cm⁻¹) and low current densities (11 and 21 mA mm⁻²) required to avoid secondary effects like Joule heating, but they did not achieve the flash regime. From this current work, noticeable effects were hard to observe below the flash regime, as, for instance, for specimens C-150 and D-300. Therefore, stronger electrical parameters were required. This is due to the different geometry of the specimen, which requires a higher power, but also to the absence of any in-situ shrinkage measurements. Obviously, the required accuracy to measure the densification of thin layers is much higher than for a 15-mm high cylinder.44 Additionally, the laser signal was heavily disturbed, probably by both the high electric field and the light emission, making the results unreliable (see Figure S1). However, we believe that even lower electric fields could have a positive effect on constrained sintering, though measuring this is technically challenging.

4.2 | Specific experimental setup and process parameters

For the flash sintering, we opted for a smaller DC power source rather than a larger AC one because of the higher accuracy in the current control. Despite using DC voltage, no clear directional gradients in microstructure were observed across the two electrodes, unlike the GDC10 dog bones in Mishra et al. 16 This can be explained by the relative long dwell times and the specific conditions at the electrode extremities. Instead of a directional gradient, we observed that under both the Pt electrodes (Figure 2B), the density was higher than the rest of the sample due to the small pressure (10 N over $\sim 1 \text{ cm}^2$, so $\sim 0.1 \text{ MPa}$) from the alumina bridge and the higher local temperature. These regions were excluded from the analysis because of these additional effects, but one exemplary image is shown in the Supplementary Information in Figure S3. Despite the application of the load by means of the alumina bridge might seem a complication of the experiment design, the reproducibility and stability of the electrical contact between electrodes and sample was definitely improved thanks to this. In principle, a strong contact is not needed because the formation of a conducting plasma between the electrodes and the sample is expected to fill small airgaps, as, for instance, discussed in Saunders et al.⁴⁷ and Sortino et al.⁴⁸ Nevertheless, the difference in the present experiment is that the sample is not between the two electrodes and, therefore, perpendicular to the electric field lines.

Regarding the key process parameters for flash sintering of thin layers, the following observations can be made:

- (i) From Figures 7–9, it appears clear that the current density is the most important parameter influencing densification, consistent with literature, such as the results on GDC10 dog bones by Mishra et al. 15
- (ii) The first experiments with specimen A (Set I) showed that achieving flash sintering required more severe conditions than those for free-hanging bulk samples.
- (iii) There are two distinct regimes based on the applied power. For specimen E-600, the maximum applied electric field is 404 V cm⁻¹ and the initial current density exceeds 620 mA mm⁻², reaching over 910 mA mm⁻² by the end. Under these conditions, a sharp increase in conductivity (or electric field drop) was observed, typical of flash sintering (Figure 6A). However, the electric field curves of specimens C-150 and D-300 do not show this abrupt change, suggesting that the provided power is insufficient for a proper onset of flash sintering.
- (iv) The experiments conducted here lasted significantly longer than typical flash sintering. However, our main objective was to demonstrate the feasibility of the process and explore the effect of current on thin layers. In Set II, the 4-h dwell time, though long, helps to differentiate better the effect of current density (goal of Set II) from that of time. By matching the dwell time across all samples, including the reference B-0, current density remains the only variable. This makes samples C-150 and D-300 particular important,

as they show that even with extended dwell time, too low current densities have a minimal impact on the microstructure.

journal

(v) The results from Set III displayed that the dwell time is a critical factor for achieving high densification. However, when the focus shifts toward sintering microstructures suitable for electrodes, high densification is no longer necessary. For example, sample G-45 already reaches a relative density above 85% after just 45 min of dwell time. Yet, for porous electrodes, ideal densities are typically in the range of 60-70% relative density, allowing for a significant reduction in dwell time.

4.3 | Comparison with literature and effect of the aspect ratio

To date, flash sintering has mainly been studied in bulk specimens (e.g., dog bones, bars, cylinders), with only two prior studies on thin films. Schwarzbach et al.⁴⁹ investigated ZnO thin films produced via a precision ion polishing system/focused ion beam or epitaxial growing on Al₂O₃ substrates. These lamellas were mounted in a Transmission Electron Microscope (TEM) for in-situ flash sintering observations and the TEM stage was heated only by Joule heating. While they directly observed flash sintering, the complex sample preparation introduced defects, complicating interpretation. Interestingly, they reported unusually high electric fields and currents, attributed to ZnO film conductivity, but without discussing geometry or substrate effects. The latter are considered in our work, as shown later in Figures 12 and 13.

Phuah et al.⁵⁰ studied GDC10 films (~185 nm), deposited onto SrTiO₃ substrates, under 900°C and 150 V cm⁻¹. Their setup is similar to ours, but smaller, with the main difference being that the middle part of our GDC10 layer is exposed to air. Their resulting current density is in the order of ~10⁵ mA mm⁻², assuming the third missing dimension being a few mm. However, they did not observe the switch to current-controlled mode, indicating that the applied power was not sufficient to trigger the typical power surge associated with flash sintering.

The comparison between these two works^{49,50} and the observations in points (ii) and (iii) of the previous Section 4.2 highlights the importance of the specimen geometry and the required power density to initiate flash sintering. In the Arrhenius plot of constant heating rate experiments, the flash onset is identified by a sudden increase in power density.³⁰ Similarly, we can calculate the power densities at their peaks and normalize by the volume. Although our experiments were conducted under isothermal conditions (less ideal than a constant heating

FIGURE 12 (A) Critical power densities for the onset of flash sintering, normalized to the volume. (B) Critical power densities for the onset of flash sintering, normalized to the surface area.

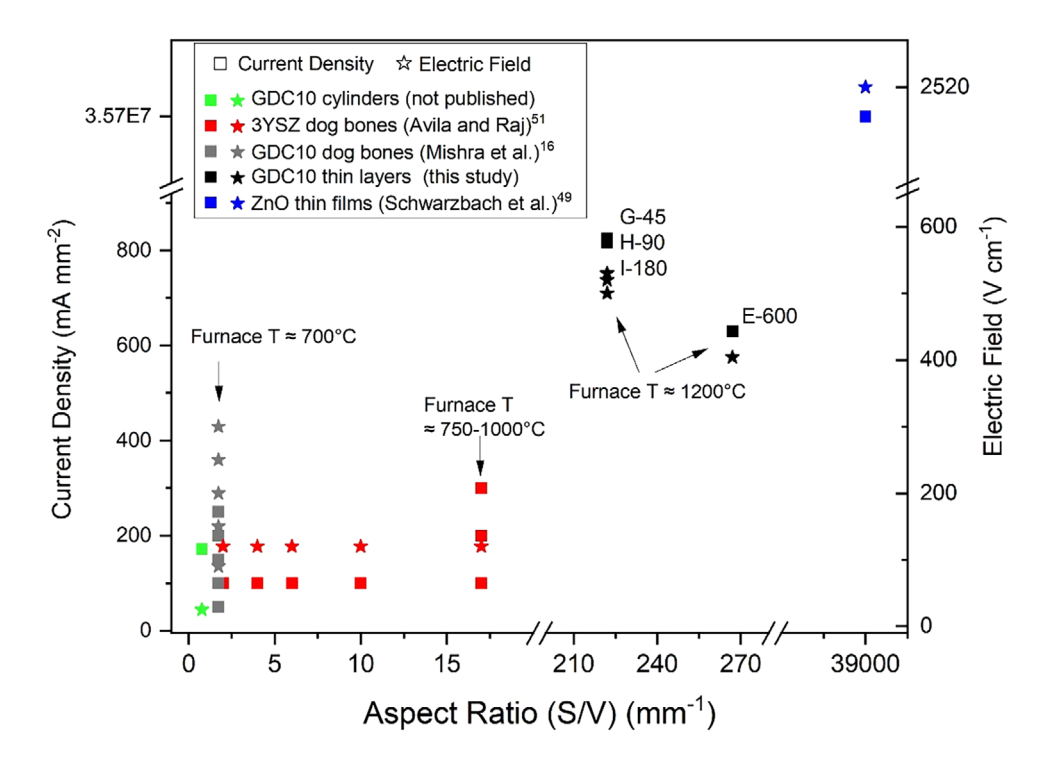


FIGURE 13 Typical current densities and electric fields used for flash sintering of specimens with different aspect ratios.

rate), the approach is conceptually similar. The power density can be calculated in Equation (4) as the product of the electric field and current density³⁰:

$$\frac{E\left(Vcm^{-1}\right)}{10} * J\left(\frac{mA}{mm^2}\right). \tag{4}$$

Using the electric fields and initial current densities from Table 2, we slightly underestimate the real power

densities since the actual values depend on the layer thickness at the power peak. Figure 12A compares the power densities for our experiments, in black squares, with those from Avila and Raj⁵¹ in red dots, and from Schwarzbach et al.⁴⁹ (blue triangle). Raj and coworkers suggest a narrow range (10–50 mW mm⁻³) of critical power densities to initiate flash sintering, irrespective of the material.^{30,52} For our thin layers, power densities are two to three times higher than those for conventional dog

journal

bones or bars, but very much lower than the ZnO thin films of Schwarbach et al. 49 (refer to their fig. 9). The major finding from Avila and Raj⁵¹ was the high dependency of the critical power density on the specimen aspect ratio, that is, the surface area to volume ratio. Higher aspect ratios corresponded to higher critical power densities. The important consequence is that the power density had to be normalized by the surface area rather than the volume. Figure 12B shows the same data as Figure 12A but is normalized by surface area, revealing a narrower power density range of 4-55 mW mm⁻², independently of the specimen geometry. The single point related to Schwarzbach et al. lays several orders of magnitude above, but this is not too surprising if the specimen aspect ratio is considered.

The aspect ratio of dog bones, bars, and cylinders ranges from 0.5 to 2, while the aspect ratio of our thin layers is between 220 and 265. The ZnO thin films in the analysis of Schwarzbach et al.⁴⁹ have an extremely high aspect ratio of about 39 000 (70 nm \times 200 nm \times 8.6 μ m). Figure 13 illustrates the typical current densities and electric fields used for flash sintering different geometries. Specimens C-150 and D-300 were excluded as they did not exhibit the characteristic power surge of flash sintering (Figure 6A). GDC10 cylinders were flash sintered with the same setup as in Cao et al.⁴⁴ Low electric field (25 V cm⁻¹) and relatively low current density (170 mA mm⁻²) were sufficient to achieve an appropriate flash onset. The results on dog bones are taken from Avila and Raj⁵¹ for 3YSZ, where the aspect ratio was intentionally varied, and from Mishra et al. for GDC10, 16 in which different combinations of parameters led to safe flash sintering.

It is also worth noting that the required furnace temperature generally increases with aspect ratio. Campos et al.⁵³ confirmed this trend, showing that for fixed electrical parameters and cylinder diameter, an increase in the specimens height (i.e., decrease in the aspect ratio) resulted in a decrease in the flash onset temperature.

As also suggested in Avila and Raj,⁵¹ the present work confirms that higher aspect ratios require extra power density necessary to balance the higher heat dissipation through large surface.

Heat loss and interpretation 4.4

Furthermore, here not only a high aspect ratio is involved, but also a distinctive configuration. In typical setups, such as free-hanging bars, dog bones, or standing cylinders, the current flows directly through the material, and heat loss mainly occurs through the specimen surface via ther-

mal radiation. Our setup differs significantly from more standard configurations: current flows into the GDC layer because alumina has much lower electrical conductivity.⁵⁴ In contrast, alumina's thermal conductivity of alumina is considerably higher than that of GDC (~30 against 1-3 W m⁻¹ K⁻¹)^{55,56} which affects overall heat conduction in the system (Figure 2B). As a result, a portion of the supplied energy dissipates through the alumina/platinum components, increasing the power required to achieve sintering. This is evident in the configuration shown in Figure 3, where high electric fields and current densities are necessary (Figure 10), despite the specimen being free-hanging.

The influence of dwell time reflects a conventional sintering behavior, where the alumina substrate is slightly further heated by the transfer of the Joule heating, resulting from the current flow in the GDC layer. We interpret the underlying physics as follows: below a certain current density, the current mainly causes local heating with a small impact on densification (as seen in samples C-150 and D-300). In this regime, the mechanism does not differ much from conventional sintering. However, once a critical threshold of current (or power) is surpassed, significant changes in microstructure and conductivity are observed (samples E and those in Set III). Despite that, the temperature increase observed in Figure 10A,B is not showing any sudden increase with the increase of current density (temperature of the substrate). Regarding temperature estimation of the GDC layer, the black body radiation model, commonly used in other flash sintering studies,⁵⁷ is not applicable due to the complexity of our setup. The experiment shown in Figure 3 required several attempts to complete successfully, primarily due to frequent loss of electric contact. While a detailed thermal analysis and modeling could provide further insight, this lies beyond the scope of the present work. We may suppose that the effect of ultra-fast firing⁵⁸ can be excluded here because of the high heat loss through the alumina substrate. However, other minor mechanisms could be involved and further analysis is required. The fact that we could not directly measure the shrinkage in-situ does not exclude an effect on v^p (Equation 3) is effectively occurring, even at high current densities/electric fields.

The electric conductivity measurements presented in Figure 11 show that the material properties were not significantly affected by the process, despite the high electric field and current density applied in sample K-cond. Unlike the "memory of flash" effect, observed by Yadav et al.⁵⁹ for titania single crystals flashed at over 450 V cm⁻¹, this phenomenon does not appear to occur in our case. The calculated activation energies (Ea) derived by the slope of $ln(\sigma T)$ versus T^{-1} are slightly higher than those in the literature. 60 The background for this increase in activation

energy can be complex and is beyond the scope of this paper. Nevertheless, the conductivities as well as E_a of both samples are comparable.

4.5 | Perspectives

In this context, the use of platinum electrodes is not ideal from an industrial perspective because it would require extra costs for the application and removal of expensive platinum. However, for basic investigations, the platinum electrodes are still a convenient solution and allow a better comparison with the previous works in literature, especially those on GDC10 by Mishra and coworkers. 15,16 To address the limitations posed by platinum electrodes, several research groups have explored the potential of contactless flash sintering (CFS), aiming at simplifying handling and optimizing the process. Lucideon Ltd. and the Imperial College London have made notable progress in this area.⁶¹ While other experimental approaches are documented in the literature, many of these setups are too complex to be scaled up from laboratory to industrial applications. Early attempts included flash sintering with arc discharge, 47 combining flames with flash sintering, 62 continuous flash sintering, 48 and an innovative concept involving two separate electric circuits—one powering the reactor and the other the induction coil for generating a magnetic field. 63,64 Another approach proposed by Dong et al.65 involves dielectric barrier discharge atmospheric cold plasma. Overall, CFS methods still require significant development before they can be implemented on an industrial scale.

5 | CONCLUSIONS

This work explored the feasibility of flash sintering of GDC10 thin layers, which were deposited onto rigid alumina substrates by an industrial-like process such as screen-printing. Literature reports rarely on thin components and is limited to very thin films for lab-scale fundamental studies. This method, despite its limitations and possible improvements, shows interesting potential for scaling up to application-oriented components for SOCs. The green layer thickness ranged from 7.5 to 9 μ m, with the other two dimensions between 8 and 15 mm, comparable to those used in small button cells.

The experiments were conducted under isothermal conditions, with the lowest furnace temperature required for flash onset being 1100° C, along with an electric field of 600 V cm $^{-1}$. For better specimen conductivity, however, a temperature of 1200° C was preferred to conduct a parametric

study. In this case, an electric field of about 500 V cm⁻¹ was enough to trigger a flash.

The current had a noticeable effect only when the current density exceeded at least 600 mA mm⁻², with more significant effects occurring above 800 mA mm⁻². The typical sudden increase in conductivity, or electric field drop, was observed only with these higher electric parameters; otherwise, the process kinetics was too slow to match the definition of flash regime (Stage II).

Relative densities above 90% were obtained at current densities over 800 mA mm⁻² and dwell times beyond 180 min. However, a shorter holding time of 45 min was sufficient to reach densities exceeding 85% TD, while conventional sintering at 1200°C for 3 h reached a densification of about 75% TD. Porous electrochemical electrodes could be sintered also in a shorter time.

The technical limitations of the power source prevented us from exploring the electric fields above 600 V cm⁻¹ and pushing the limits of the process toward lower temperatures. The available maximum current was more than sufficient for such thin layers, but had to be precisely tuned to avoid extreme high current densities and sample failure. After layer shrinkage, the final current densities reached values between 1000 and 1300 mA mm⁻², with the Joule heating effect being clearly observed under these conditions.

Interestingly, the required electric parameters were generally much higher than those needed to flash sinter bulk GDC, a result attributed to the significantly higher surface area-to-volume ratio and the specific experiment configuration, which caused greater heat loss also toward the substrate. Despite the demanding conditions, particularly the high electric field, the electric properties of the flash-sintered specimens were comparable to those of CS specimens. Further studies are needed to explore a broader range of parameters and to better understand the mechanisms at play in this specific type of specimen.

For industrial applications, the need for electrode contact remains a key challenge. Thin layers with large surface areas could benefit from the development of advanced CFS, which is still in its early stages.

ACKNOWLEDGMENTS

The authors acknowledge funding from the German Science Foundation (DFG), under the priority program "Fields Matter" SPP 1959 (grants nos. BR 3418/1-2 and GU 933/9-2), and from the Austrian Science Fund (FWF) (grant no. 10.55776/I5478). Additionally, the authors want to thank Prof. Rajendra K. Bordia for the useful discussions.

Open access funding enabled and organized by Projekt DEAL.

ORCID

Luca Balice https://orcid.org/0000-0003-3664-6797 Christian Melcher https://orcid.org/0009-0005-4173-1306

Alexander Opitz https://orcid.org/0000-0002-2567-1885

Martin Bram https://orcid.org/0000-0002-1203-2777

Olivier Guillon https://orcid.org/0000-0003-4831-5725

REFERENCES

- Jacobson AJ. Materials for solid oxide fuel cells. Chem Mater. 2010;22(3):660-74. https://doi.org/10.1021/cm902640j
- Minh NQ. Ceramic fuel cells. J Am Ceram Soc. 1993;76(3):563– 88. https://doi.org/10.1111/j.1151-2916.1993.tb03645.x
- Zheng Y, Wang J, Yu B, Zhang W, Chen J, Qiao J, et al. A review of high temperature co-electrolysis of H2O and CO2 to produce sustainable fuels using solid oxide electrolysis cells (SOECs): advanced materials and technology. Chem Soc Rev. 2017;46(5):1427-63. https://doi.org/10.1039/C6CS00403B
- Häfele S, Hauck M, Dailly J. Life cycle assessment of the manufacture and operation of solid oxide electrolyser components and stacks. Int J Hydrog Energy. 2016;41(31):13786–96. https://doi.org/10.1016/j.ijhydene.2016.05.069
- Menzler NH, Tietz F, Uhlenbruck S, Buchkremer HP, Stöver D. Materials and manufacturing technologies for solid oxide fuel cells. J Mater Sci. 2010;45(12):3109–35. https://doi.org/10.1007/ s10853-010-4279-9
- Green DJ, Guillon O, Rödel J. Constrained sintering: a delicate balance of scales. J Eur Ceram Soc. 2008;28(7):1451–66. https:// doi.org/10.1016/j.jeurceramsoc.2007.12.012
- Brandner M, Bram M, Froitzheim J, Buchkremer HP, Stöver D. Electrically conductive diffusion barrier layers for metal-supported SOFC. Solid State Ion. 2008;179(27):1501–4. https://doi.org/10.1016/j.ssi.2008.03.002
- Biesuz M, Sglavo VM. Flash sintering of ceramics. J Eur Ceram Soc. 2019;39(2):115–43. https://doi.org/10.1016/j.jeurceramsoc. 2018.08.048
- Wu J, Wu X, Gao Y, Yan Z. Innovations in electric currentassisted sintering for SOFC: a review of advances in flash sintering and ultrafast high-temperature sintering. Appl Sci. 2024;14(10):3953. https://doi.org/10.3390/app14103953
- Jiang T, Liu Y, Wang Z, Sun W, Qiao J, Sun K. An improved direct current sintering technique for proton conductor— BaZr0.1Ce0.7Y0.1Yb0.1O3: the effect of direct current on sintering process. J Power Sources. 2014;248:70–76. https://doi.org/10.1016/j.jpowsour.2013.09.042
- Sun K, Zhang J, Jiang T, Qiao J, Sun W, Rooney D, et al. Flash-sintering and characterization of La0.8Sr0.2Ga0.8Mg0.2O3-δ electrolytes for solid oxide fuel cells. Electrochimica Acta. 2016;196:487–95. https://doi.org/10.1016/j.electacta.2016.02.207
- 12. Cologna M, Rashkova B, Raj R. Flash sintering of nanograin zirconia in <5 s at 850°C. J Am Ceram Soc. 2010;93(11):3556–59. https://doi.org/10.1111/j.1551-2916.2010.04089.x
- 13. Cologna M, Prette ALG, Raj R. Flash-sintering of cubic yttriastabilized zirconia at 750°C for possible use in SOFC manufacturing. J Am Ceram Soc. 2011;94(2):316–19. https://doi.org/10. 1111/j.1551-2916.2010.04267.x
- 14. Francis JSC, Cologna M, Montinaro D, Raj R. Flash sintering of anode–electrolyte multilayers for SOFC applications. J

- Am Ceram Soc. 2013;96(5):1352–54. https://doi.org/10.1111/jace.
- Mishra TP, Neto RRI, Raj R, Guillon O, Bram M. Current-rate flash sintering of gadolinium doped ceria: microstructure and defect generation. Acta Mater. 2020;189:145–53. https://doi.org/ 10.1016/j.actamat.2020.02.036
- Mishra TP, Lenser C, Raj R, Guillon O, Bram M. Development of a processing map for safe flash sintering of gadolinium-doped ceria. J Am Ceram Soc. 2021;104(9):4316–28. https://doi.org/10. 1111/jace.17847
- 17. Eguchi K, Setoguchi T, Inoue T, Arai H. Electrical properties of ceria-based oxides and their application to solid oxide fuel cells. Solid State Ion. 1992;52(1):165–72. https://doi.org/10.1016/0167-2738(92)90102-U
- Bowman WJ, Zhu J, Sharma R, Crozier PA. Electrical conductivity and grain boundary composition of Gd-doped and Gd/Pr co-doped ceria. Solid State Ion. 2015;272:9–17. https://doi.org/10.1016/i.ssi.2014.12.006
- 19. Guillon O., editor. *Advanced ceramics for energy conversion and storage*. The Netherlands: Elsevier Ltd.; 2020.
- Bishop SR, Duncan KL, Wachsman ED. Defect equilibria and chemical expansion in non-stoichiometric undoped and gadolinium-doped cerium oxide. Electrochimica Acta. 2009;54(5):1436–43. https://doi.org/10.1016/j.electacta.2008.09.
- Hussain S, Yangping L. Review of solid oxide fuel cell materials: cathode, anode, and electrolyte. Energy Transit. 2020;4(2):113– 26. https://doi.org/10.1007/s41825-020-00029-8
- Udomsilp D, Rechberger J, Neubauer R, Bischof C, Thaler F, Schafbauer W, et al. Metal-supported solid oxide fuel cells with exceptionally high power density for range extender systems. Cell Rep Phys Sci. 2020;1(6):100072. https://doi.org/10.1016/j. xcrp.2020.100072
- Nenning A, Holzmann M, Fleig J, Opitz AK. Excellent kinetics of single-phase Gd-doped ceria fuel electrodes in solid oxide cells. Mater Adv. 2021;2(16):5422–31. https://doi.org/10.1039/D1MA00202C
- Uecker J, Unachukwu ID, Vibhu V, Vinke IC, Eichel R-A, (Bert) De Haart LGJ. Performance, electrochemical process analysis and degradation of gadolinium doped ceria as fuel electrode material for solid oxide electrolysis cells. Electrochimica Acta. 2023;452:142320. https://doi.org/10.1016/j.electacta.2023. 142320
- 25. Uecker J, Unachukwu ID, Vibhu V, Vinke IC, (Bert) de Haart LGJ, Eichel R-A. Gadolinium doped ceria as nickel–free fuel electrode in high temperature CO2-electrolysis. ChemElectroChem. 2024;11(7):e202300617. https://doi.org/10.1002/celc.202300617
- Bance P, Brandon NP, Girvan B, Holbeche P, O'Dea S, Steele BCH. Spinning-out a fuel cell company from a UK University—2 years of progress at Ceres Power. J Power Sources. 2004;131(1):86–90. https://doi.org/10.1016/j.jpowsour. 2003.11.077
- Bone A, Leah R, Matthews C, Lankin M, Rahman M. Electrolyte forming process. Withers & Rogers LLP Patent, GB 2524640. 2015.
- 28. Kumar MKP, Yadav D, Lebrun J-M, Raj R. Flash sintering with current rate: a different approach. J Am Ceram Soc. 2019;102(2):823–35. https://doi.org/10.1111/jace.16037

155 12916, 2025, 10, Downloaded from https://ceramics.onlinelibrary.wiley.com/doi/10.1111/jace.70033 by Forschungszentrum

Jülich GmbH Research Center, Wiley Online Library on [20/08/2025]. See the Terms

on Wiley Online Library for rules of use; OA articles are governed by the applicable Creative Commons

- 29. Hao X, Liu Y, Wang Z, Qiao J, Sun K. A novel sintering method to obtain fully dense gadolinia doped ceria by applying a direct current. J Power Sources. 2012;210:86-91. https://doi.org/10.1016/j. ipowsour.2012.03.006
- 30. Raj R. Analysis of the power density at the onset of flash sintering. J Am Ceram Soc. 2016;99(10):3226-32. https://doi.org/10. 1111/jace.14178
- 31. Valdebenito JU, Akbari-Fakhrabadi A, Viswanathan MR. Effect of flash sintering on microstructure of Ce0.9Gd0.1O1.95 electrolyte fabricated by tape-casting. Mater Lett. 2017;209:291-94. https://doi.org/10.1016/j.matlet.2017.07.129
- 32. Spiridigliozzi L, Biesuz M, Dell'Agli G, Di Bartolomeo E, Zurlo F, Sglavo VM. Microstructural and electrical investigation of flashsintered Gd/Sm-doped ceria. J Mater Sci. 2017;52(12):7479-88. https://doi.org/10.1007/s10853-017-0980-2
- 33. Guillon O, Aulbach E, Rödel J, Bordia RK. Constrained sintering of alumina thin films: comparison between experiment and modeling. J Am Ceram Soc. 2007;90(6):1733-37. https://doi.org/ 10.1111/j.1551-2916.2007.01650.x
- 34. Aulbach E, Zuo R, Rödel J. Laser-assisted high-resolution loading dilatometer and applications. Exp Mech. 2004;44(1):71-75. https://doi.org/10.1007/BF02427979
- 35. Cao C, Mücke R, Wakai F, Guillon O. Viscous Poisson's ratio, bulk and shear viscosity during electrical field assisted sintering of polycrystalline ceria. Scr Mater. 2020;178:240-43. https://doi. org/10.1016/j.scriptamat.2019.11.043
- 36. Dash A, Morita K, Balice L, Mücke R, Guillon O. Creep and superplasticity of gadolinium-doped ceria ceramics under AC electric current. Adv Eng Mater. 2023;25(18):2300057. https:// doi.org/10.1002/adem.202300057
- 37. Francis JSC, Raj R. Flash-sinterforging of nanograin zirconia: field assisted sintering and superplasticity. J Am Ceram Soc. 2012;95(1):138-46. https://doi.org/10.1111/j.1551-2916.2011.04855.
- 38. Francis JSC, Raj R. Influence of the field and the current limit on flash sintering at isothermal furnace temperatures. J Am Ceram Soc. 2013;96(9):2754-58. https://doi.org/10.1111/jace.12472
- 39. Nicholas JD, De Jonghe LC. Prediction and evaluation of sintering aids for cerium gadolinium oxide. Solid State Ion. 2007;178(19):1187-94. https://doi.org/10.1016/j.ssi.2007.05.019
- 40. M'Peko J-C, Francis JSC, Raj R. Impedance spectroscopy and dielectric properties of flash versus conventionally sintered yttria-doped zirconia electroceramics viewed at the microstructural level. J Am Ceram Soc. 2013;96(12):3760-67. https://doi. org/10.1111/jace.12567
- 41. Vendrell X, Yadav D, Raj R, West AR. Influence of flash sintering on the ionic conductivity of 8 mol% yttria stabilized zirconia. J Eur Ceram Soc. 2019;39(4):1352-58. https://doi.org/10.1016/j. jeurceramsoc.2018.12.048
- 42. Lai W, Haile SM. Impedance spectroscopy as a tool for chemical and electrochemical analysis of mixed conductors: a case study of ceria. J Am Ceram Soc. 2005;88(11):2979-97. https://doi.org/ 10.1111/j.1551-2916.2005.00740.x
- 43. Nenning A, Opitz A. Low oxygen partial pressure increases grain boundary ion conductivity in Gd-doped ceria thin films. J Phys Energy. 2019;2(1):014002. https://doi.org/10.1088/2515-7655/ab3f10
- 44. Cao C, Mücke R, Guillon O. Effect of AC field on uniaxial viscosity and sintering stress of ceria. Acta Mater. 2020;182:77-86. https://doi.org/10.1016/j.actamat.2019.10.035

- 45. Scherer GW, Garino T, Viscous sintering on a rigid substrate, J Am Ceram Soc. 1985;68(4):216-20. https://doi.org/10.1111/j.1151-2916.1985.tb15300.x
- 46. Bordia RK, Scherer GW. On constrained sintering—I. Constitutive model for a sintering body. Acta Metall. 1988;36(9):2393–97. https://doi.org/10.1016/0001-6160(88)90189-7
- 47. Saunders T, Grasso S, Reece MJ. Ultrafast-contactless flash sintering using plasma electrodes. Sci Rep. 2016;6(1):27222. https:// doi.org/10.1038/srep27222
- 48. Sortino E, Lebrun J-M, Sansone A, Raj R. Continuous flash sintering, J Am Ceram Soc. 2018;101(4):1432-40, https://doi.org/10. 1111/jace.15314
- 49. Schwarzbach D, Gonzalez-Julian J, Guillon O, Roddatis V, Volkert CA. Towards in-situ electron microscopy studies of flash sintering. Ceramics. 2019;2(3):472-87. https://doi.org/10.3390/ ceramics2030036
- 50. Phuah XL, Wang H, Qi Z, Misra S, Kalaswad M, Wang H. Fieldassisted heating of Gd-doped ceria thin film. J Am Ceram Soc. 2020;103(4):2309-14. https://doi.org/10.1111/jace.16949
- 51. Avila V, Raj R. Flash sintering of ceramic films: the influence of surface to volume ratio. J Am Ceram Soc. 2019;102(6):3063-69. https://doi.org/10.1111/jace.16298
- 52. Raj R, Wolf DE, Yamada CN, Jha SK, Lebrun J-M. On the confluence of ultrafast high-temperature sintering and flash sintering phenomena. J Am Ceram Soc. 2023;106(7):3983-98. https://doi. org/10.1111/jace.19070
- 53. Campos JV, Lavagnini IR, Pereira da Silva JG, Ferreira JA, Sousa RV, Mücke R, et al. Flash sintering scaling-up challenges: influence of the sample size on the microstructure and onset temperature of the flash event. Scr Mater. 2020;186:1-5. https:// doi.org/10.1016/j.scriptamat.2020.04.022
- 54. Peters DW, Feinstein L, Peltzer C. On the high-temperature electrical conductivity of alumina. J Chem Phys. 1965;42:2345-46. https://doi.org/10.1063/1.1696298
- 55. Hemrick J, Kistler C Jr, Wereszczak A, Ferber M. Thermal conductivity of alumina measured with three techniques. J Test Eval. 2003;31(5):438-42. https://doi.org/10.1520/JTE12368J
- 56. Muthukkumaran K, Kuppusami P, Srinivasan Ramachandran K. Thermal properties of 15-mol% gadolinia doped ceria thin films prepared by pulsed laser ablation. Ionics. 2007; 13:47–50. https://doi.org/10.1007/s11581-007-0068-0
- 57. Raj R. Joule heating during flash-sintering. J Eur Ceram Soc. 2012;32(10):2293-301. https://doi.org/10.1016/j.jeurceramsoc. 2012.02.030
- 58. Ji W, Parker B, Falco S, Zhang JY, Fu ZY, Todd RI. Ultra-fast firing: effect of heating rate on sintering of 3YSZ, with and without an electric field. J Eur Ceram Soc. 2017;37(6):2547-51. https://doi.org/10.1016/j.jeurceramsoc.2017.01.033
- 59. Yadav D, Yuan Y, Gopalan V, Raj R, Jo S. Room temperature flash of single crystal titania: electronic and optical properties. J Am Ceram Soc. 2023;106(1):46-52. https://doi.org/10.1111/jace.
- 60. Swanson M, Tangtrakarn N, Sunder M, Moran PD. Impact of the presence of grain boundaries on the in-plane ionic conductivity of thin film Gd-doped CeO2. Solid State Ion. 2010;181(8):379-85. https://doi.org/10.1016/j.ssi.2010.01.020
- 61. Kassem R, Jones GM, Green CD, Al Nasiri N. Development of environmental barrier coatings using novel flash sintering technique. J Eur Ceram Soc. 2025;45(1):116807. https://doi.org/10. 1016/j.jeurceramsoc.2024.116807

journal

- 62. Johnson SL, Venugopal G, Hunt AT. Flame-assisted flash sintering: a noncontact method to flash sinter coatings on conductive substrates. J Am Ceram Soc. 2018;101(2):536-41. https://doi.org/ 10.1111/jace.15218
- 63. Jalali SIA, Raj R. Touch-free flash sintering with magnetic induction within a reactor activated by the usual flash method. J Am Ceram Soc. 2022;105(11):6517–22. https://doi.org/10.1111/ jace.18601
- 64. Çetinkaya Z, Raj R. Processing map for touch-free flash sintering of a whiteware ceramic. J Am Ceram Soc. 2024;107(9):5720-27. https://doi.org/10.1111/jace.19875
- 65. Dong J, Wang Z, Zhao X, Biesuz M, Saunders T, Zhang Z, et al. Contactless flash sintering based on cold plasma. Scr Mater. 2020;175:20-23. https://doi.org/10.1016/j.scriptamat.2019.08.039

SUPPORTING INFORMATION

Additional supporting information can be found online in the Supporting Information section at the end of this article.

How to cite this article: Balice L, Dash A, Melcher C, Sebold D, Mücke R, Opitz A, et al. Constrained flash sintering of gadolinium-doped ceria thin layers. J Am Ceram Soc. 2025;108:e70033. https://doi.org/10.1111/jace.70033